https://doi.org/10.5194/egusphere-2024-2565
Preprint. Discussion started: 3 September 2024

A Data-Efficient Deep Transfer Learning Framework for Methane Super-Emitter Detection in Oil and Gas Fields Using Sentinel-2 Satellite

Shutao Zhao[1,2], Yuzhong Zhang[2,3]*, Shuang Zhao[2,3], Xinlu Wang[1,2], Daniel J. Varon[4]

1. College of Environmental & Resource Sciences, Zhejiang University, Hangzhou, Zhejiang Province, 310058, China
2. Key Laboratory of Coastal Environment and Resources of Zhejiang Province, School of Engineering, Westlake University, Hangzhou, Zhejiang Province, 310024, China
3. Institute of Advanced Technology, Westlake Institute for Advanced Study, Hangzhou 310024, Zhejiang Province, China
4. School of Engineering and Applied Sciences, Harvard University, Cambridge, United States

Corresponding Author: Yuzhong Zhang, *Email: zhangyuzhong@westlake.edu.cn;

Abstract

Efficiently detecting large methane point sources (super-emitters) in oil and gas fields is crucial for informing stakeholders for mitigation actions. Satellite measurements by multispectral instruments, such as Sentinel-2, offer global and frequent coverage. However, methane signals retrieved from satellite multispectral images are prone to surface and atmospheric artifacts that vary spatially and temporally, making it challenging to build a detection algorithm that applies everywhere. Hence, laborious manual inspection is often necessary, hindering widespread deployment of the technology. Here, we propose a novel deep-transfer-learning-based methane plume detection framework. It consists of two components: an adaptive artifact removal algorithm (low reflectance artifact detection, LRAD) to reduce artifacts in methane retrievals, and a deep subdomain adaptation network (DSAN) to detect methane plumes. To train the algorithm, we compile a dataset comprising 1627 Sentinel-2 images from 6 known methane super-emitters reported in the literatures. We evaluate the ability

https://doi.org/10.5194/egusphere-2024-2565
Preprint. Discussion started: 3 September 2024

of the algorithm to discover new methane sources with a suite of transfer tasks, in which training and evaluation data come from different regions. Results show that the DSAN (average macro-F1 score 0.86) outperforms two convolutional neural networks (CNN), MethaNet (average macro-F1 score 0.7) and ResNet-50 (average macro-F1 score 0.77), in transfer tasks. The transfer-learning algorithm overcomes the issue of conventional CNNs that their performance degrades substantially in regions outside training data. We apply the algorithm trained with known sources to an unannotated region in the Algerian Hassi Messaoud oil field and reveal 34 anomalous emission events during a one-year period, which are attributed to 3 methane super-emitters associated with production and transmission infrastructure. These results demonstrate the potential of our deep-transfer-learning-based method towards efficient methane super-emitter discovery using Sentinel-2 across different oil and gas fields worldwide.

Keywords

Methane; Oil and gas field; Super-emitter; Sentinel-2; Deep transfer learning

https://doi.org/10.5194/egusphere-2024-2565
Preprint. Discussion started: 3 September 2024

1 Introduction

As one of the most important greenhouse gases, methane (CH4) constitutes approximately a quarter of the overall global warming since the preindustrial age as reported by (IPCC, 2013). Among all the sources, reducing methane emissions from anthropogenic sources, including from oil and gas (O&G) production, is vital for mitigating near-term climate change (Lauvaux et al. 2022). Methane emission in the O&G production sector comes from point emitters such as malfunctioning flares, wells, storage tanks, and gas compressor stations. These point emissions exhibit to be a long-tailed distribution, that is, a substantial fraction of the total emissions are contributed by a limited number of anomalous point sources, which often linked with production equipment malfunctions or abnormal operating conditions (Zavala-Araiza et al. 2017; Duren et al. 2019). Therefore, efficiently detecting these anomalous methane point sources is crucial for informing prompt mitigation actions.

Atmospheric methane concentrations can be quantified remotely by measuring backscattered radiation at wavelengths (e.g., around 1700 nm and 2150 nm) that correspond to the rotational-vibrational resonances of methane molecular transitions (Ehret et al. 2022). Recent studies demonstrated that both multispectral and hyperspectral satellite instruments have the capability to identify anomalous methane point emissions (Guanter et al. 2021; Varon et al. 2021; Sánchez-García et al. 2022). Hyperspectral instruments (e.g., GHGSat, PRISMA, EMIT, and GF-5) offer higher sensitivity to CH4 and thus lower point source detection limit owing to their fine spectral resolution, but hyperspectral observations generally exhibit sparsity in both spatial and temporal coverage (Naus et al. 2023; Pandey et al. 2023). In comparison, multispectral satellites (including Landsat-8, WorldView-3, and Sentinel-2) provide global,

https://doi.org/10.5194/egusphere-2024-2565
Preprint. Discussion started: 3 September 2024

frequent, and spatially continuous observations, though their sensitivity to methane is lower because of coarse spectral resolution (Varon et al. 2021; Ehret et al. 2022). As an illustration, Sentinel-2 provides global coverage data on a weekly basis, spanning a period of eight years. Detection limit of the Sentinel-2 measurements for methane gas in the atmosphere is roughly 5000 kg/h or greater for heterogeneous surfaces (Gorroño et al. 2023).

However, the routine scanning for methane super-emitters across varied O&G areas remains challenging primarily due to the lack of an efficient automated source detection algorithm (Fig. 1). Currently, source detection predominantly relies on human visual inspection, a process that is time- and labor- consuming, thereby impeding the large-scale deployment (Jongaramrungruang et al. 2022; Schuit et al. 2023). Deep learning techniques have been proposed to develop point-source detectors for airborne instruments (Jongaramrungruang et al. 2022), satellite area mappers (e.g., TROPOMI) (Schuit et al. 2023), and satellite hyper/multispectral instruments (e.g., PRISMA, Sentinel-2) (Bruno et al. 2023; Joyce et al., 2023; Vaughan et al. 2023).

One of the key challenges in constructing such an automated detector for multispectral observations is the low signal-to-noise ratio (SNR) in the retrieved methane signals. Because of the coarse spectral resolution, methane signals obtained from multispectral observations are susceptible to diverse artifacts, including interferences from vegetation, water bodies, and smoke, making source detection a difficult task, especially over heterogenous land surface (Cusworth et al. 2019). To mitigate these artifacts, several filtering strategies have been proposed, such as background pixel removal (Guanter et al. 2021; Varon et al. 2021) or worst predicted pixel removal (Ehret et al. 2022).

https://doi.org/10.5194/egusphere-2024-2565
Preprint. Discussion started: 3 September 2024

Another challenge arises from the necessity for an efficient detector to rapidly identify small-scale methane point emissions in satellite data with large-scale (global) coverage. Existing automated detectors for high-spatial-resolution satellites (Bruno et al. 2023; Joyce et al., 2023; Vaughan et al. 2023) performed pixel-level detection which classified each pixel in an image as plume-containing or plume-free. However, multispectral satellites such as Sentinel-2 have high detection limits for methane emissions, even more than 5000 kg/h for heterogeneous surfaces (Gorroño et al. 2023). This means that the retrieved images containing methane plumes are extremely rare on both spatial and temporal scales within Sentinel-2 observations, as evidenced by Ehret et al. (2022). So far, a relatively small number of super-emitters have been detected by multispectral satellite, mainly in desertic regions with bright, uniform surfaces (Varon et al. 2021; Ehret et al. 2022; Irakulis-Loitxate et al. 2022; Sánchez-García et al. 2022; Naus et al. 2023; Pandey et al. 2023). In contrast, O&G production is spread across ~ 100 countries worldwide, often with distinct environments (EIA; https://www.eia.gov), resulting in different noise and artifact characteristics. Therefore, an image-level detector is required to efficiently filter out the myriad of methane-free patches. To this end, deep transfer learning becomes a valuable strategy towards constructing a data-efficient detection model using a limited volume of real training data (Jiang et al. 2022), without the need to construct large simulated datasets (Jongaramrungruang et al. 2022; Radman et al. 2023). Utilizing the inherent resemblance between the source and target domains, a deep transfer learning technique can adapt the learned feature distribution acquired from a source data/task to a target data/task during the training process (Iman et al. 2023).

In this work, we aim to improve methane source detection using Sentinel-2 observations.

https://doi.org/10.5194/egusphere-2024-2565
Preprint. Discussion started: 3 September 2024

We develop an adaptive artifact detection and masking algorithm that enhances the signal-to-noise ratio for retrieved methane signals, and a deep transfer learning method that improves detection efficiency and performance of discovering unknown sources, leveraging knowledge acquired from known methane sources. To train our method, we also construct a dataset of Sentinel-2 methane retrievals comprising Sentinel-2 detectable super-emitters reported in literature. Our method is a step forward towards large-scale operational monitoring of methane super-emitters by multispectral satellite instruments.

2 Methodology

2.1 Satellite data

We employ the Sentinel-2 Level 1C (L1C) top-of-atmosphere reflectance product, which is freely available through [https://dataspace.copernicus.eu]. The Copernicus Sentinel-2 mission is composed of two polar-orbiting satellites: Sentinel-2A, launched on June 23, 2015, and Sentinel-2B, launched on March 7, 2017. The mission can provide global coverage data with a revisit time of 2-5 days and a swath width of 290 km. The MultiSpectral Instruments (MSIs) onboard Sentinel-2 incorporates 13 channels spanning the visible and near-infrared spectra, featuring spatial resolutions that vary between 10 to 60 m. Sentinel-2 data have been used to support a variety of applications including land management, natural resource monitoring, and risk mapping (Ienco et al. 2019; Ramoelo et al. 2015; Varghese et al. 2021). Recent studies demonstrated the potential of Sentinel-2 to monitor methane super-emitters (Ehret et al. 2022; Gorroño et al. 2023; Radman et al. 2023; Varon et al. 2021; Vaughan et al.

https://doi.org/10.5194/egusphere-2024-2565
Preprint. Discussion started: 3 September 2024

2023). Here, we use bands 11 (1610 nm) and 12 (2190 nm) for methane signal retrieval and bands 3 (560 nm), 8 (842 nm), and 11 (1610 nm) for artifact filtering. We resample the data to 20-m resolution using the ESA snap-python toolbox and discard scenes with cloud coverage greater than 80%.

To train our algorithm, we collect Sentinel-2 observations in the vicinity of six O&G methane sources (indexed as #1-#6) where reoccurring ultra-emissions have been reported (Irakulis-Loitxate et al. 2022; Sánchez-García et al. 2022; Varon et al. 2021; Zhang et al. 2022). Table 1 summarizes the information about these methane sources, which are located in five oil and gas fields differing substantially in surrounding terrain and surface characteristics. These O&G sources also differ in the types of emitting facilities (e.g., compressor station, flare, well pad, and pipeline) and the magnitude of emission fluxes (2-100 t/h) (Table 1). To construct our training dataset, we use Sentinel-2 tile 40SBH during March 2017 to March 2023 for emitter #1, #2, and #3, tile 32SKA from January 2019 to December 2022 for emitter #4 and #5, and tile 13SGR from January 2018 to December 2020 for emitter #6 (Table 3). We crop the original Sentinel-2 data to generate patches of 16 km^2 in size, which are then used by our algorithm.

Table 1 Reported methane super-emitters detected by multispectral satellite instruments.

Index	Emitter [a]	Ordinates	O&G field	Land cover [b]	Country	Emission flux range (kg/h) [c]	References
#1	Compressor station	(38.19393°, 54.19764°)	Korpeje	Barren area	Turkmenistan	3500-92900 (08/2015-10/2020)	(Varon et al. 2021)
#2	Flare	(38.33078°, 54.02832°)	Gamyshlja Gunorta	Barren area	Turkmenistan	≥ 1800 (01/2017-11/2020)	(Irakulis-Loitxate et al. 2022)
#3	Flare	(37.90825°, 53.89857°)	Keymir	Barren area and Grass land	Turkmenistan		
#4	Well-pad device	(31.6585°, 5.9053°)	Hassi Messaoud	Barren area	Algeria	2600-29100 (10/2019-09/2020)	(Varon et al. 2021)
#5 [d]	Pipeline	(31.778°, 5.995°) (31.768°, 6.000°)	Hassi Messaoud	Barren area	Algeria	3100 (12/29/2020) 2500 (12/29/2020)	(Sánchez-García et al. 2022)

https://doi.org/10.5194/egusphere-2024-2565
Preprint. Discussion started: 3 September 2024

#6	Compress or station	(31.7335°, -102.0421°)	Permian basin	Shurbland	U.S.	2360-21830 (07/2020-09/2020)	(Zhang et al. 2022)

[a] Reports of these sources are all based on Sentinel-2 data expect for #5 which is based on Worldview-3.

[b] Land cover type near the emitter is obtained from the annual ESA/CCI land cover map 2020 [https://maps.elie.ucl.ac.be/CCI/viewer/index.php] as a reference. It is noted that the land cover map has a spatial resolution of 300 m, which cannot reflect surface features smaller than an area of 300 m^2.

[c] Values in this column represent emission flux during the time range or date studied in literatures. It is noted that the emission flux of emitter #2-3 has not been reported by (Irakulis-Loitxate et al. 2022), and 1800 kg/h is the detection limit of Sentinel-2 provided in the literature.

[d] Emitter #5 contains two pipeline leakage sources approximately 1.2 km apart. They are numbered together since they are only around 60 pixels apart in the 20m resolution Sentinel-2 image.

2.2 Framework for multispectral satellite point source detection and quantification

Fig. 1 shows the workflow of methane super-emitter monitoring using Sentinel-2 satellite data, with algorithms developed in this study highlighted in red text. The workflow primarily includes three steps, methane signal retrieval, source detection, and flux quantification.

First, methane signals are retrieved from satellite measurements. We employ the structural similarity index measure (SSIM) algorithm (Zhou et al. 2004) to filter out cloudy observations and the low-reflectance adaptive detection (LRAD) algorithm developed in this study (Section 2.3) to filter out other interference. We then compute fractional methane absorption signal (ΔR, unitless) using band 11 and 12 from Sentinel-2 (Ehret et al. 2022; Irakulis-Loitxate et al. 2022):

$$\Delta R^{t} = \frac{\mathrm{band}_{12}^{\mathrm{t}}/\mathrm{band}_{12}^{\mathrm{ref}}}{\mathrm{band}_{11}^{\mathrm{t}}/\mathrm{band}_{11}^{\mathrm{ref}}}$$

where $\mathrm{band}_{12}^{\mathrm{t}}$ and $\mathrm{band}_{11}^{\mathrm{t}}$ represent observations on the date of interest (t) and $\mathrm{band}_{12}^{\mathrm{ref}}$ and $\mathrm{band}_{11}^{\mathrm{ref}}$ represent reference conditions without any methane enhancement. We borrow the idea of sliding time window in Ehret et al. (2022) to predict $\mathrm{band}_{12}^{\mathrm{ref}}$ and $\mathrm{band}_{11}^{\mathrm{ref}}$ by the multivariate linear regression (MLR) model trained on band 11 and 12 observations in the time window (within 60 days prior to date t). Data excluded by SSIM and LRAD are not used for the MLR model training. See Text S1 for detailed information on the methane signal retrieval step.

Second, we train an automated detector to detect potential methane super-emitters based on

https://doi.org/10.5194/egusphere-2024-2565
Preprint. Discussion started: 3 September 2024

retrieved ΔR, in place of human inspection. We annotate ΔR images retrieved from Sentinel-2 observations of 6 methane super-emitters (Table 1). The dataset is then used to train and evaluate a deep subdomain adaptation network (DSAN) (Section 2.4) to detect whether an image contains methane plumes. Our work demonstrates that the DSAN detector, trained with a relatively small number of annotated ΔR images, shows promising performance in unknown source detection.

Finally, we quantify emission fluxes (kg/h) of detected methane plumes by employing the Integrated Mass Enhancement (IME) method (Frankenberg et al. 2016; Varon et al. 2018). See Text S2 for detailed descriptions about the flux quantification method.

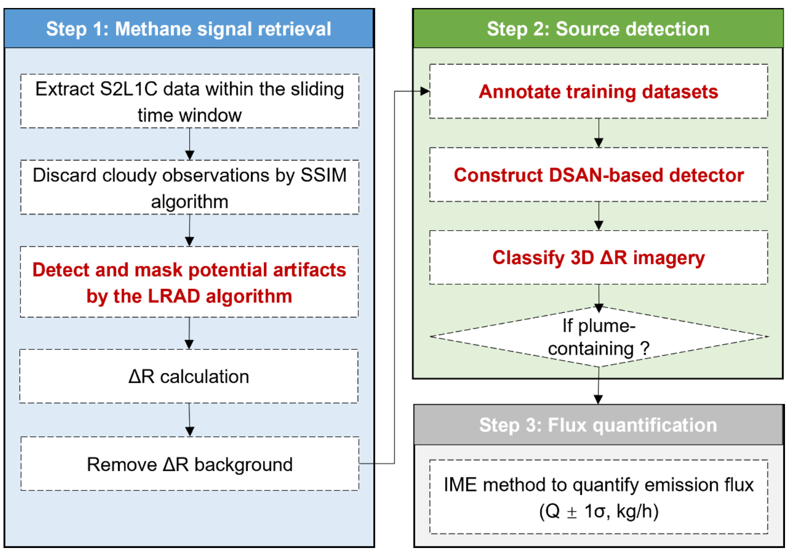

Fig. 1. The methane super-emitter monitoring workflow (from Sentinel-2 L1C product to emission flux of the detected methane point emission signal). Text in red highlights the novel algorithms developed in this study.

2.3 Low reflectance artifact detection (LRAD) algorithm for artifact removal

To increase the signal-to-noise ratio of Sentinel-2 methane retrieval, we develop a low reflectance artifacts detection (LRAD) algorithm to identify and remove varied artifacts associated with low reflectance in the methane-sensitive band by surface features. Figure 2 (a) and (b) show examples of these potential artifacts resulting from varied surface elements including smoke (from burning flare), rocky soil (with high mineral content), dark soil (with high organic matter or water content), water body, cloud shadow, and vegetation (Gorroño et al. 2023; Naus et al. 2023). These artifacts in the SWIR bands may be filtered out by leveraging additional bands that are sensitive to the artifacts but insensitive to methane (Figure 2(c)).

Fig. 3 shows the pseudocode of the LRAD algorithm, which creates a surface artifact mask using Band 3 (560 nm), 4 (665 nm), and 8 (842 nm), in addition to Band 11 and 12. For combustion-related artifacts, the algorithm first filters out pixels with saturated reflectance in Band 11 and 12, which are related to thermal anomalies from high-temperature combustion (Liu et al. 2021). The algorithm then filters out pixels affected by heavy smoke, identifiable by extraordinarily low visible-band reflectance in Band 3 (the 5% lowest values of the scene). We calculate the standard deviation σ and then apply the 2σ (around 95% confidence interval) as the masking threshold. The above mask is then dilated to ensure that interference from combustion sources is removed.

Additionally, the LRAD algorithm filters out pixels with concurrent negative values of the Normalized Difference Vegetation Index (NDVI) (Band 8 and Band 4) and the Normalized Difference Built-up Index (NDBI) (Band 8 and Band 11), which are related to low-reflectance objects in SWIR such as water bodies (Biermann et al. 2020; Fan et al. 2020; Purio et al. 2022). Positive values of these indices have been used in literature to detect healthy vegetation and urban areas (Kuc and Chormański 2019).

https://doi.org/10.5194/egusphere-2024-2565
Preprint. Discussion started: 3 September 2024

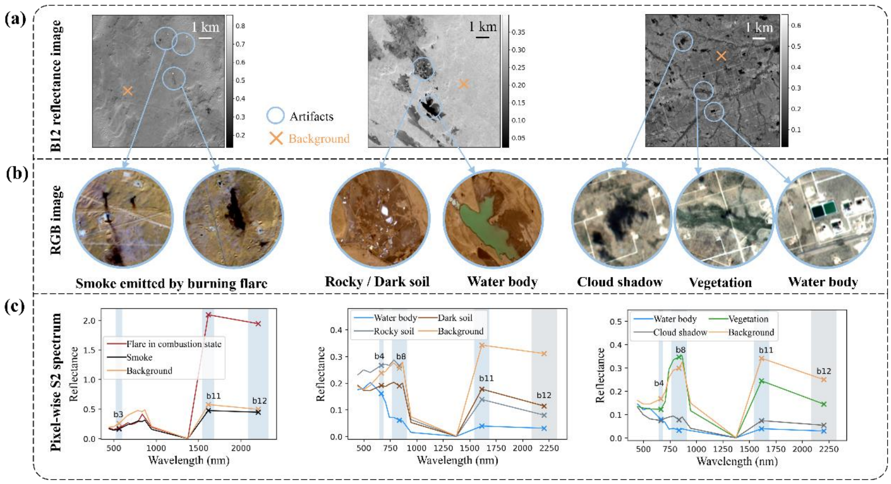

Fig. 2. Examples of varied artifacts in Sentinel-2 (S2) L1C reflectance images. (a) S2L1C band 12 (b12) reflectance images in Hassi Messaoud (20190117T32SKA), Gamyshlja Gunorta (20200404T40SBH), and Permian basin (20190126T13SGR). (b) Representative RGB images of the artifacts presenting low reflectance in b12. (c) Pixel-wise S2L1C reflectance spectrum of the background and representative artifacts. Bands used for identifying artifacts are shown in blue shadings.

Algorithm Low reflectance artifacts detecting (LRAD) algorithm

Input: Data cube X with size of $m \times n \times 5$ is extracted from S2L1C product, each pixel i in X has 5 wavelength bands including b_3, b_4, b_8, b_{11}, and b_{12}.

Output: $Mask$

Initialize $Mask = Ones(m \times n)$
for all i **do**
  if ($b_{11}^i \geq 1.0$ & $b_{12}^i \geq 1.0$) **then** //Detect flare in combustion state
    $Mask[i] = 0$ //Filter pixels containing flare
    $Mask[where\ (b_3 \leq Quantile_{b_3}^{5\%})] = 0$ //Filter pixels containing smoke
  end if
  $NDVI = (b_8 - b_4)/(b_8 + b_4)$; $NDBI = (b_{11} - b_8)/(b_{11} + b_8)$
  $Mask[where\ (NDVI \leq 0) \cup where\ (NDBI \leq 0)] = 0$
  //Filter pixels containing artifacts with low reflectance in NIR and SWIR bands
end for
$Mask = Dilation\ (Mask)$
return $Mask$

Fig. 3. LRAD algorithm to generate the mask for low reflectance artifacts in methane retrieval bands (Band 11 and 12) using data in Band 3, 4, and 8.

2.4 Deep transfer learning for methane source detection

We employ the deep subdomain adaptation network (DSAN) (Zhu et al. 2021) to detect the presence of methane plumes in retrieved ΔR images (Fig. 4). DSAN is a transfer learning

https://doi.org/10.5194/egusphere-2024-2565
Preprint. Discussion started: 3 September 2024

algorithm that leverages feature representations acquired from a labeled source domain to enhance performance on the unlabeled target domain (Pan and Yang 2010). By using DSAN, we attempt to address the challenge that a methane-source classifier trained with labeled data in one location (source domain) tends to perform inadequately in another location where labeled data are unavailable (target domain), because of great differences in surface characteristics between regions (domain shift).

Fig. 4 illustrates the structure of DSAN applied in this study. DSAN consists of deep feature extraction blocks and a domain adaptation module. Feature extraction is done by adapting a pre-trained residual neural network (ResNet-50) as the backbone of DSAN. ResNet-50 has demonstrated exceptional performance in various image classification tasks, especially those based on spatial context, largely because of its strong feature mining capability enabled by shortcut connections (Burke et al. 2021) (see Fig. S2). ResNet-50 consists of 16 residual blocks that contain a series of convolutional layers and shortcut connections. Following each convolutional layer, there is a subsequent batch normalization layer and a Rectified Linear Unit (ReLU) activation function.

The domain adaptation module transforms deep features extracted by ResNet-50 to align the feature distributions between source and target domains. The alignment is performed based on local maximum mean discrepancy (LMMD), which measures the distance between feature distributions (Zhu et al. 2021). The general form of LMMD is presented as:

$$LMMD(P,Q) = \frac{1}{N}\sum_{i=1}^{N}\left\| E_P^i[\phi(D_s^i)] - E_Q^i[\phi(D_t^i)]\right\|_H^2$$

Where D_s and D_t are the samples in source and target domain, P and Q are the probability distribution of D_s and D_t, and i is the class of the sample (plume-containing or plume-free).

https://doi.org/10.5194/egusphere-2024-2565
Preprint. Discussion started: 3 September 2024

LMMD is designed to capture both global (whole dataset) and local (each class) domain differences, and therefore is sensitive to variability within each class. This property is important for our application because the difference between the two classes (plume-containing and plume-free ΔR images) are more subtle compared to a typical image classification task.

The DSAN is first trained using labelled ΔR images in the source domain and unlabeled ΔR images in the target domain, before it is used to predict labels for target-domain images. The input ΔR imagery is transformed to match the ResNet-50 (which serves as the backbone of DSAN) input format. Before feeding into the network (Fig. 4), the input image was resized to 224*224, augmented by randomly flipping the images horizontally during the training process, and then normalized to ensure that the three channels had a consistent scale. The model is trained with a learning rate of 0.001 using stochastic gradient descent (SGD) optimizer over 100 epochs.

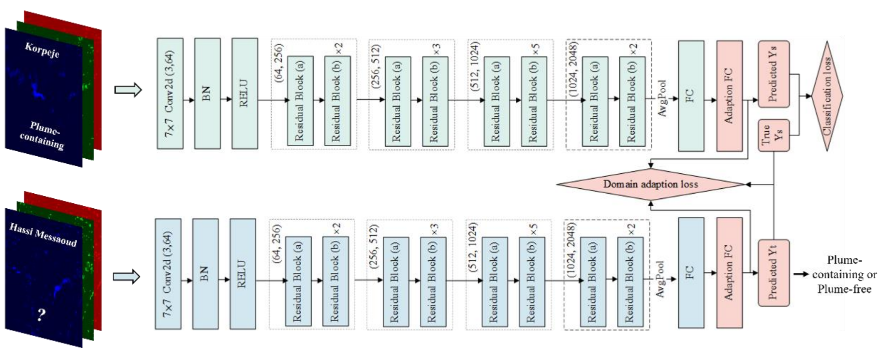

Fig. 4. The architecture of DSAN. DSAN employs ResNet-50 to learn features from labeled (green) and unlabeled (blue) data, and then the domain adaptation module (red) to reduce the domain distribution discrepancy.

2.5 Experiment design

2.5.1 Performance evaluation on transfer tasks

We design two experiments (Fig. S4) to evaluate the performance of the DSAN framework

https://doi.org/10.5194/egusphere-2024-2565
Preprint. Discussion started: 3 September 2024

in detecting unknown sources, using 6 ΔR datasets corresponding to the 6 super-emitters (denoted as #1-6; Table 1) for training and evaluation. Table 2 describes the training, validation, and test subsets separation ways. In the first experiment (‘1→1’ task), we use one of the six datasets as the source domain (labels available to the algorithm) and another dataset as the target domain (labels unavailable to the algorithm and to be predicted). In total, there are 6×5=30 ‘1→1’ tasks to be evaluated. In the second experiment (‘5→1’ task), we use five of the six datasets as the source domain and the remaining one as the target domain, which yields six ‘5→1’ tasks. The ‘1→1’ tasks examine how well a detector constructed based on data from a known source can discover unknown sources, while the ‘5→1’ tasks evaluate whether and to what degree performance can be enhanced by including training data from multiple sources.

To compare, we also build two convolutional neural networks (CNNs) (Fig. S3) based on MethaNet (Jongaramrungruang et al. 2022) and ResNet-50, which, unlike DSAN, do not contain a domain adaptation module. For each ‘1→1’ or ‘5→1’ task, a CNN methane-source detector is trained with the labeled source-domain dataset(s) before being applied to predict the labels for the target domain. We train the MethaNet model from scratch and the ResNet-50 model with a fine-tuning strategy demonstrated by (Radman et al. 2023).

Table 2 Training, validation, and test subsets separation for different types of models and tasks.

Model	Task	Training set	Validation set	Test set
DSAN	‘1→1’, ‘5→1’	source domain	---	target domain
MethaNet and ResNet-50	‘1→1’, ‘5→1’	80% source domain	20% source domain	target domain
	non-transfer	80% source domain	20% source domain	---

The performance is assessed for each task with accuracy, precision, recall, and the macro-F1-score using the scikit-learn package (Pedregosa et al. 2011). The main metric we use is the macro-F1 score, computed as the average of F1 scores for each class (harmonic mean of precision and recall). The macro-F1 score has a range of 0-1, suitable for datasets with

https://doi.org/10.5194/egusphere-2024-2565
Preprint. Discussion started: 3 September 2024

imbalanced positive and negative samples. A higher macro-F1 score indicates a better overall performance. Additional metrics encompass accuracy, representing the ratio of correctly predicted instances to the total instances; precision, calculated as the number of true positive predictions divided by the total number of positive predictions; and recall, determined by dividing the number of true positive predictions by the total number of actual positive instances.

2.5.2 Real-world application for new source discovery

To test in a real-world scenario, we apply the proposed workflow (Fig. 1) to the Hassi Messaoud O&G field in Algeria. We randomly select an orbit (for tile T32SKA) in this region which covers an area of 4×108 km^2 during July 2019-June 2020. The original data are segmented and converted into 200px × 200px patches (an area of ~16 km^2), generating a total of 3537 cloud-free ΔR images in the region. We use these unannotated data as the target domain for DSAN and the labeled datasets described above (#1-#6) as the source domain. Finally, the results predicted by the detector are evaluated against manually determined labels.

3. Methane retrieval (ΔR) imagery dataset

We compile ΔR datasets containing six super-emitters reported in the literatures (Table 1) using Sentinel-2 L1C observations. Each sample in the dataset consists of a ΔR image retrieved from the original satellite data (Step 1 in Fig.1) and a label determined manually indicating the presence or absence of methane sources (plume-containing or plume-free).

The ΔR images of the dataset are processed with the LRAD algorithm (Section 2.4). Fig. 5 shows examples of artifact masks generated by LRAD and compares the ΔR images with and without applying the masks. This result demonstrates that the algorithm can detect and remove varied types of surface artifacts, including dark soil, rocky soil, water body, burning flare,

https://doi.org/10.5194/egusphere-2024-2565
Preprint. Discussion started: 3 September 2024

smoke plume, vegetation, and cloud shadow. Fig. S6 presents additional examples that LRAD generates masks that are adaptive to temporal changes in land covers, thus capable of detecting seasonally varying artifacts. As shown in Fig. 5, removing of these artifacts by the LRAD algorithm enhances signal-to-noise ratios (SNRs) (defined as $SNR = 20 * \log_{10}(avg./std.)$, $avg.$ and $std.$ are calculated from the entire ΔR image) in ΔR images by 12.12-42.30%, facilitating the following source detection step. Fig. S7 compares the averaged SNRs of the six ΔR datasets before and after deploying the LRAD algorithm.

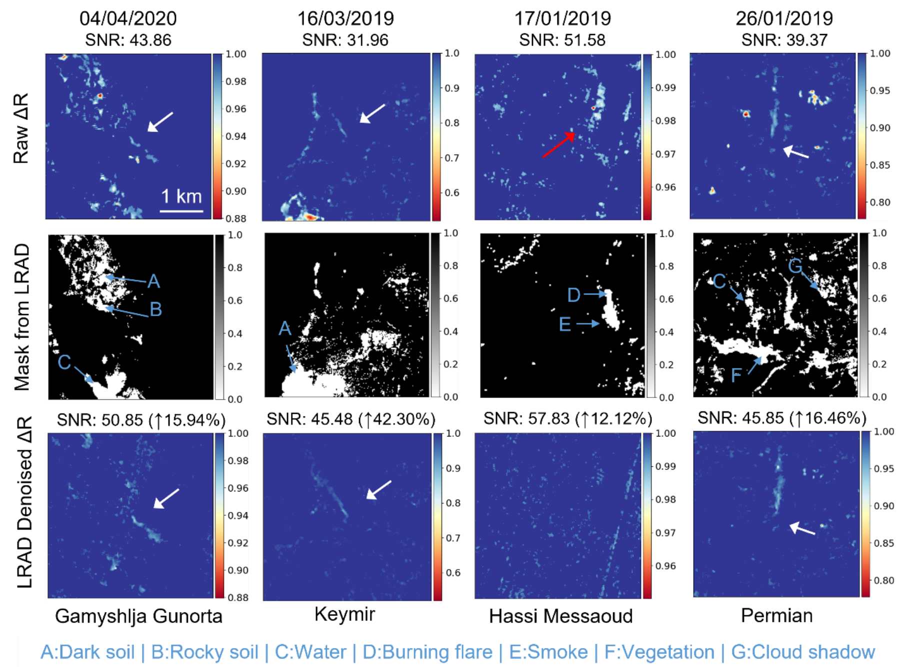

Fig. 5. Examples of the ΔR images and masks. The first row showed the raw ΔR images outputted by Step 1 procedures (Fig. 1) without LRAD deployed, the second row displayed the latent artifacts masks generated by LRAD algorithm, and the third row exhibited the denoised ΔR images outputted by Step 1 procedures (Fig. 1) with the LRAD performed. White arrows indicated true methane plumes, and red arrow indicated plume-like artifacts. Blue characters and arrows in the binary masks pointed to different types of the latent artifacts.

We label the ΔR image following the decision rule as described in Fig. 6 and Text S3. Table 3 summarizes the information of the methane imagery dataset retrieved from Sentinel-2 L1C

https://doi.org/10.5194/egusphere-2024-2565
Preprint. Discussion started: 3 September 2024

data. The dataset consists of subsets of 6 super-emitters reported in the literature (Table 1). Each subset contains 200-400 samples. These subsets differ greatly in the ratio between positive (plume-containing) and negative (plume-free) samples, ranging from 8.1% in #6 to 81.95% in #1, reflecting large variations in emission frequencies among varied sources. Most of the positive samples contain one methane plume, except for #5 in which occasionally two methane plumes are present simultaneously. We quantify the emission rates of positive samples using the IME method (Text S2) (Fig. S5). The average emission flux varies from 1952 kg/h in #5 to 17122 kg/h in #3. Moreover, the background noises exhibit considerable variations among the six subsets (Fig. 7). Subsets #1, #4, and #5 present uniform noises originating from homogeneous surfaces yet subsets #2, #3, and #6 have greater heterogeneity resulting in a higher occurrence of artifacts.

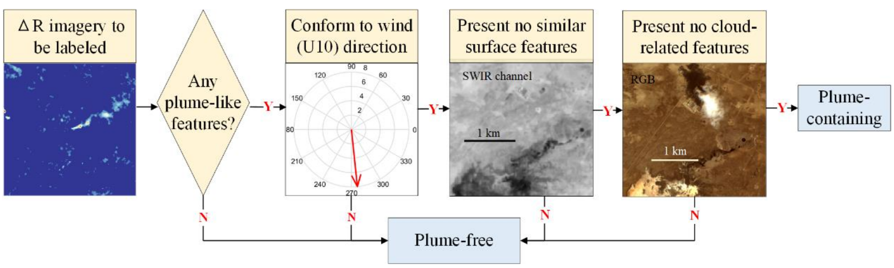

Fig. 6. A flowchart of the labeling decision rule of ΔR imagery (Detailed description is provided in Text S3).

Table 3 Description of the six labelled ΔR datasets.

Index	Sentinel-2 tile ID	Time span	Number of plume-containing observations	Number of plume-free observations	Average emission flux (kg/h)
#1			109	133	11076
#2	T40SBH	03/2017-03/2023	95	164	8826
#3			66	186	17122
#4	T32SKA	01/2019-12/2022	92	233	5717
#5			128	181	1952
#6	T13SGR	01/2018-12/2020	18	222	14443

https://doi.org/10.5194/egusphere-2024-2565
Preprint. Discussion started: 3 September 2024

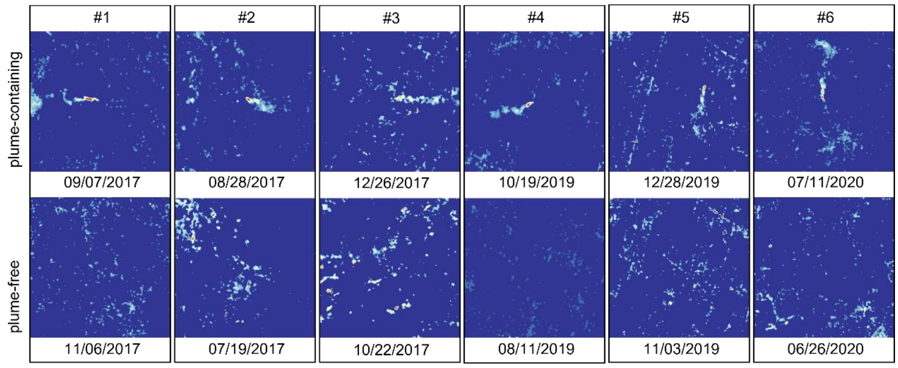

Fig. 7. Examples of the plume-containing and plume-free images in ΔR datasets #1-#6.

4. Performance evaluation of the DSAN model

Fig. 8 evaluates the ability of the DSAN model to detect a methane source in an unannotated region (transferability) with the macro-F1 scores achieved for varied '1→1' or '5→1' transfer tasks (Section 2.5.1). To compare with conventional CNNs, Fig. 9 shows results of MethaNet and ResNet-50 for the same tasks. In addition to macro-F1 scores, Table S1-S3 also tabulate other performance metrics from the experiments including accuracy, precision, and recall.

The DSAN model achieves average macro-F1 scores of 0.86 (0.69 to 0.93) for the '1→1' tasks and 0.89 (0.77 to 0.94) for the '5→1' tasks (Fig. 8), which consistently outperforms both MethaNet (0.70 for '1→1' tasks and 0.76 for '5→1' tasks) (Fig. 9(a)) and ResNet-50 (0.77 for '1→1' tasks and 0.81 for '5→1' tasks) (Fig. 9(b)). The performance of conventional CNN models degrades substantially in these transfer tasks (off-diagonal of Fig. 9), compared to non-transfer tasks (training and validation data from the same locations) (average macro-F1 scores are 0.87 for MethaNet and 0.95 for ResNet-50) (diagonal of Fig. 9), demonstrating the challenges of transfer tasks. Moreover, the performance of CNNs in '5→1' tasks (rightmost column of Fig. 9), only marginally improved over their performance in '1→1' tasks (left six columns of Fig. 9), is still inferior to DSAN's performance in most '1→1' tasks (Fig. 8), which

https://doi.org/10.5194/egusphere-2024-2565
Preprint. Discussion started: 3 September 2024

indicates that including a limited number of training samples from diverse regions is insufficient for conventional CNNs to enhance their transferability, underscoring the value of the transfer learning algorithm such as DSAN.

The disparity of the performance presented above can be interpreted by comparing the deep features extracted by MethaNet, ResNet-50, and DSAN. Fig. 10 maps high-dimensional deep features to a 2-dimentional plot generated by the t-distributed stochastic neighbor embedding (t-SNE) algorithm (Laurens van der Maaten and Hinton 2008). Blue points are source domain samples and orange points are target domain samples. DSAN exhibits better alignment between the source and the target domains compared to MethaNet and ResNet-50. In the DSAN subfigures, it is evident that not only are the source and target points well-aligned, but samples belonging to different classes also exhibit noticeable distinctions. This result is consistent with our understanding that the domain transfer module in the DSAN model can effectively close background differences between different regions (domain shift), enhancing the ability of the algorithm to identify methane plumes at a new location.

Fig. 8 and Fig. 9 also indicates that some of the datasets appear more difficult to predict than others. The DSAN's performance for dataset #2 and #6 is not as good as for other datasets (Fig. 8), while MethaNet performs poorly for dataset #2, #5, and #6 and ResNet-50 performs poorly for dataset #2 and #6 (Fig. 9). Some dataset characteristics may have contributed to lower performance. Dataset #2 is marked by highly heterogeneous surface, Dataset #5 by smaller methane fluxes and plume sizes, and Dataset #6 by higher surface complexity and imbalanced positive / negative classes (Fig. 7 and Table 3).

Increasing the source domain from one dataset ('1→1' tasks) to five ('5→1' tasks) slightly

https://doi.org/10.5194/egusphere-2024-2565
Preprint. Discussion started: 3 September 2024

improves the performance of the DSAN model (Fig. 8), demonstrating the benefit of including more and diverse training samples. However, #6 remains the most difficult dataset with no improvement.

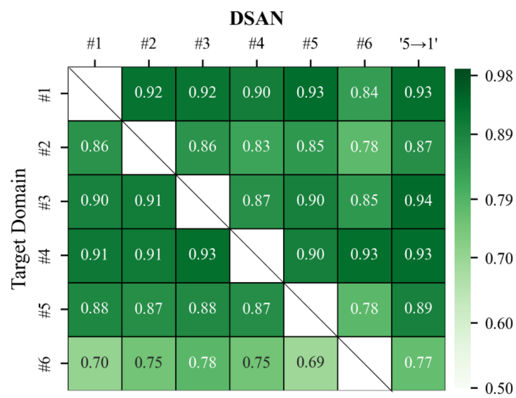

Fig. 8. Macro-F1 scores on the transfer tasks given by DSAN. Each square represents a transfer task. '5→1' represents the source domain is fused by five datasets except for the target domain dataset.

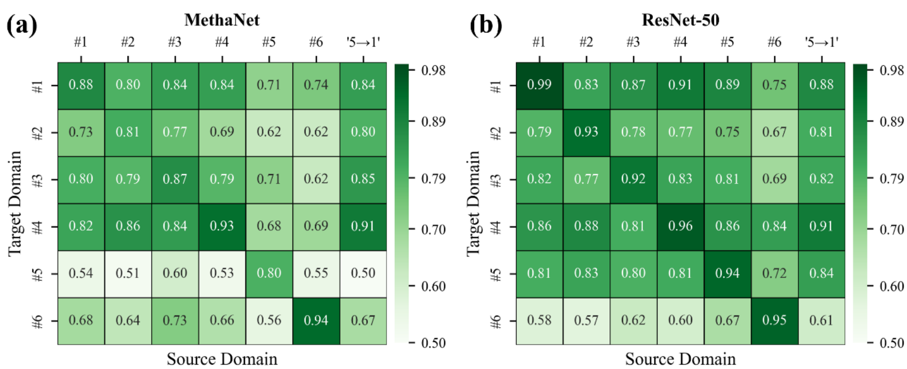

Fig. 9. Macro-F1-scores given by (a) MethaNet and (b) ResNet-50. Each square represents a task. Tasks on the diagonal pertain to non-transfer tasks, with each dataset partitioned into a training set (80%) and a validation set (20%). Tasks outside the diagonal are transfer tasks. '5→1' denotes that the source domain is fused by five datasets except for the target domain dataset.

https://doi.org/10.5194/egusphere-2024-2565
Preprint. Discussion started: 3 September 2024

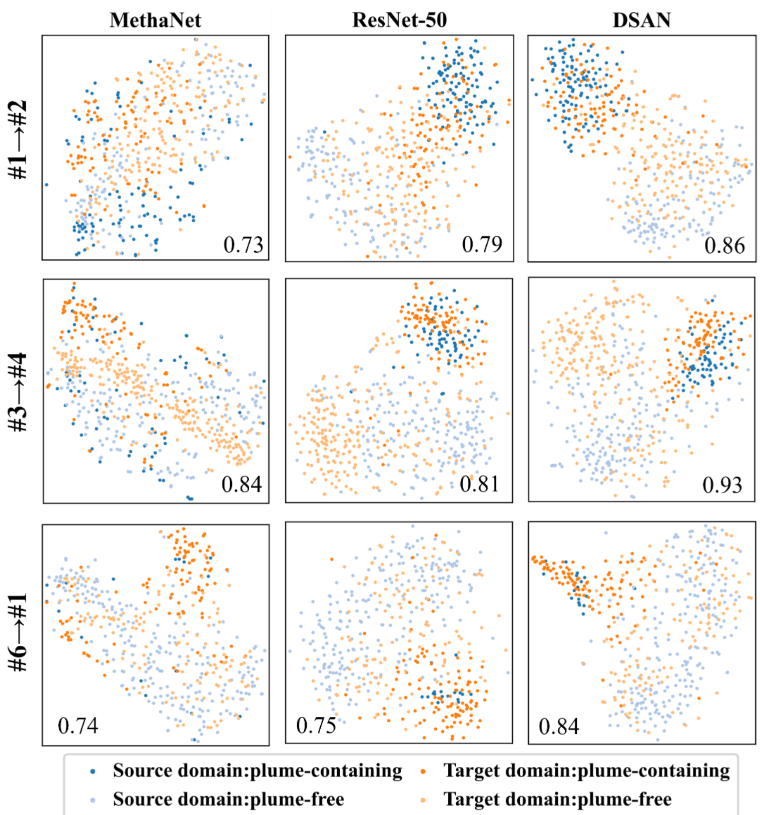

Fig. 10. t-SNE visualizations of the learned feature representations of the ΔR datasets across different models and transfer tasks, providing insights into domain shift and how well the well-trained models identify different classes in the target domain. From the left to right column: MethaNet, ResNet-50, and DSAN on three '1→1' transfer tasks (#1→#2, #3→#4, and #6→#1). Each point represents a data sample. The number in each subfigure denotes the macro-F1 score of the target domain label predicted by the model.

5. Real-world application for methane source discovery

We apply the proposed AI-assisted monitoring workflow (Fig. 1), including the LRAD and DSAN algorithms, to a 432 km^2 area (Fig. 11) in the Hassi Messaoud O&G field in Algeria (Section 2.5.2). The algorithm processed in total 3527 images (200 pixel by 200 pixel) for one year, yielding 3168 negative (plume-free) and 369 positive (plume-containing) detections.

We manually verified that 33 out of the 369 positive detections contain true methane plumes from three methane super-emitters (denoted as P(1), P(2), and P(3) in Fig. 11) and that 1 false

https://doi.org/10.5194/egusphere-2024-2565
Preprint. Discussion started: 3 September 2024

negative detection was identified at P(2) (see Fig. S8). Using the Google Earth Map, we attributed P(1) to a production well (31.8651°N, 6.1683°E) and P(2) to pipeline leakage (31.7566°N, 6.1864°E). We did not identify OG infrastructure associated with P(3) (31.5846°N, 6.4878°E) from the Google Earth Map. Fig. 11 presents visual imagery of each source and the true positive plumes detected by our method. These super-emitters were not known at the time of our experiment. Two recent studies reported P(1) based also on Sentinel-2 data (Naus et al. 2023; Pandey et al., 2023).

Methane plumes are detected twice at P(1), 30 times at P(2), and twice at P(3) during July 2019 to June 2020 (Fig. 12), resulting in respective detection frequencies of 1.6%, 24%, and 1.6% for the three sources after cloudy days are excluded. Meanwhile, the LRAD algorithm detects flaring as a byproduct (Fig. S9). We detected 67 flaring events at P(1) and one flaring event at P(2) (Fig. 12). Flaring detection at P(1) occurs primarily during July to August 2019 and January to May 2020.

We quantified the emission fluxes of the three sources using the IME method (Varon et al. 2021) (see Text S2 for details about the method). The average emission rate is 31133 kg h^{-1} for P(1), 3990 kg h^{-1} for P(2), and 8210 kg h^{-1} for P(3) (Fig. 12). The largest emissions were found at P(1) due to a blowout event with 18421±6575 kg h^{-1} on January 4, 2020 and 43845 ±9169 kg h^{-1} on January 7, 2020. This result is generally comparable to estimates given by Pandey et al. (2023) (21000±6000 kg h^{-1} on January 4) and Naus et al. (2023) (29800±14900 kg h^{-1} on January 4 and 68400±34200 kg h^{-1} on January 7).

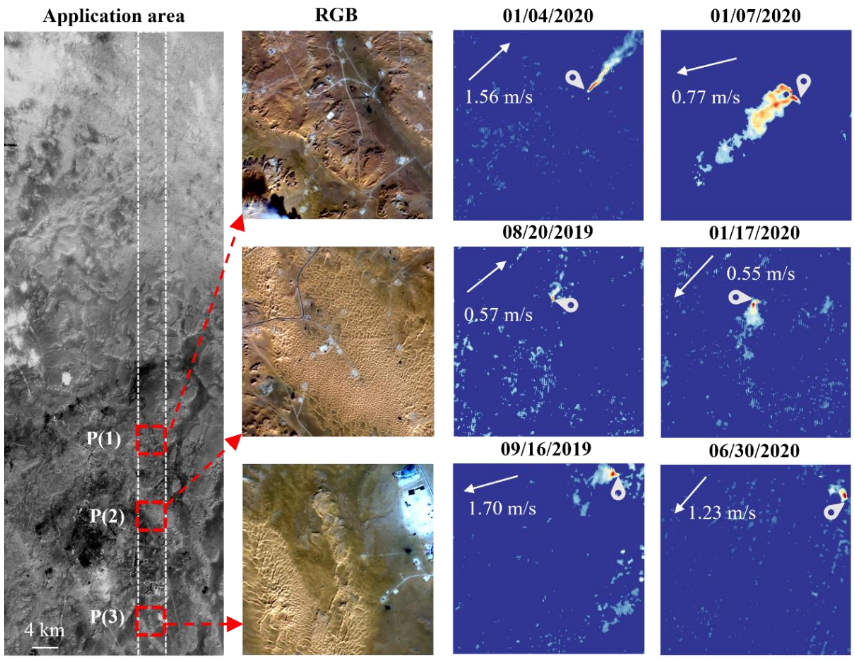

P(1): 31.8651°, 6.1683° | P(2): 31.7566°, 6.1864° | P(3): 31.5846°, 6.4878°

Fig. 11. From left to right: Application area (the rectangular area within the white dotted line) extracted from Sentinel-2 data, RGB images of the positive patches containing methane point sources (P(1)-P(3)), and examples of the methane plume-containing ΔR images detected by our method. The white pin in ΔR image points to the source location.

https://doi.org/10.5194/egusphere-2024-2565
Preprint. Discussion started: 3 September 2024

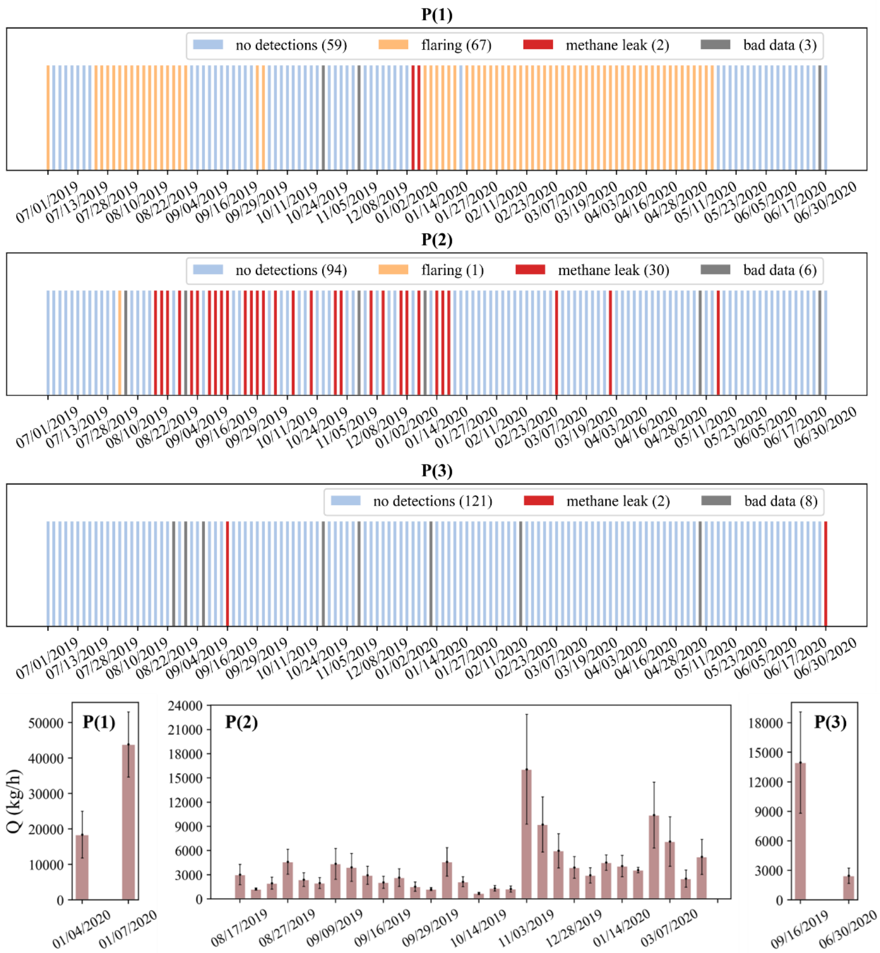

Fig. 12. Time series of the detected methane leaking events, flaring, and the retrieved emission flux of the methane plumes for P(1), P(2) and P(3). It is noted that detected methane leaks and flaring come from different facilities, and the flare burn dates do not coincide with the leak dates. No detections indicate methane-free and flaring-free. Bad data mainly indicates cloudy data or data that is fully covered by artifacts.

Table 4 summarizes the performance metrics for the real-world application. Our algorithm demonstrates a good detection capability with an accuracy of 0.90, consistent with the averaged value for the 36 transfer tasks (section 4.1.1). This performance surpasses the detection accuracy of approximately 0.80 reported by the CH4Net which used Sentinel-2 for the west coast of Turkmenistan (Vaughan et al. 2024). For 3168 plume-free images, the DSAN detector

https://doi.org/10.5194/egusphere-2024-2565
Preprint. Discussion started: 3 September 2024

achieves a false positive rate of 0.096 (FP / TN+FP), higher than the results of existing detectors tested on synthetic datasets (Zortea et al. 2023; Rouet-Leduc and Hulbert 2024). Nonetheless, this rate is lower than the 0.14 reported by the U-Plume detector on GHGSat-C1 observations (Bruno et al. 2023) and the 0.18 reported by (Vaughan et al. 2024).

Additionally, our detector shows the macro-F1 score of 0.56, which is lower than that reported in Section 4 for the evaluation tasks primarily due to the 336 false positive detections. Further analyses suggest that these false positives are related to smoke, built-up, land surface, and cloud/cloud-shadow (Fig. 13(a)). We categorize these false positives based on the type of main artifacts (Fig. 13(b)). Artifacts related to land-surface variability accounts for 77.61% of the false positives, followed by those related to cloud or cloud shadow (19.10%), and smoke (3.28%). These results indicate that some artifacts remain after processed by the artifact-removal algorithm LRAD. Investigation into these artifacts, particularly those by land surfaces, is key to further improving the performance.

Table 4 Manual validation of detections by the AI-assisted framework.

07/2019 - 06/2020	TP[a]	FP[b]	TN[c]	FN[d]	Precision	Recall	Macro-F1 score	Accuracy
All 3537 patches of the swath	33	336	3167	1	0.09 1.00	0.97 0.90	0.56	0.90

[a-d] TP (true positive), FP (false positive), TN (true negative), and FN (false negative) represent specific categories of predictions

https://doi.org/10.5194/egusphere-2024-2565
Preprint. Discussion started: 3 September 2024

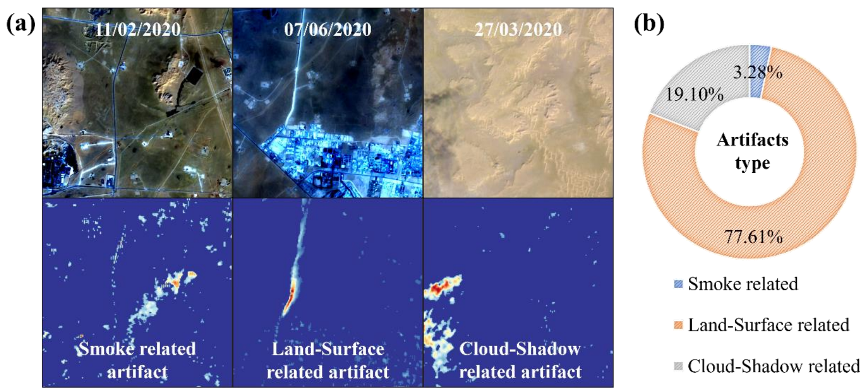

Fig. 13. False positive detection in the real-world application. (a) Representative examples of the false positive results, and the corresponding RGB images extracted from Sentinel-2 L1C product; (b) Contributions of various artifact types to false positive detections.

6. Discussion

6.1 Comparison with existing denoising methods

Noise and artefacts in retrieved ΔR imagery poses significant challenges to real-world image classification tasks such as satellite-based methane plume detection, impacting the convergence and generalization of deep neural networks (Dodge and Karam 2016). Table 5 summarizes existing denoising methods. To reduce noises, Varon et al. (2021) proposed to remove outliers using 3×3 median filter algorithm and remove background noises below 95% confidence interval. Similarly, Ehret et al. (2022) discarded the 5% worst predicted pixels obtained from methane-free background estimation and then apply a Gaussian filter. Furthermore, Zortea et al. (2023) generated a binary mask to exclude the water-body-related artifacts using the MNDWI. These denoising methods performed well on relatively homogeneous surfaces, where noise is uniformly distributed and artefacts are small in area and infrequent in time. However, in heterogeneous regions, such as those shown in the first and last columns of Fig. 5, artifacts are more prominent and often cover areas larger than those of the

https://doi.org/10.5194/egusphere-2024-2565
Preprint. Discussion started: 3 September 2024

methane plumes, making them more challenging to address by existing denoising methods. Utilizing additional spectral bands, our LRAD algorithm is designed to address multiple types of artifacts and is adaptive to different types of land surfaces. As illustrated in Fig. S6, LRAD generates large-area denoising masks for heterogeneous surfaces and small-area or even no masks for homogeneous regions. The effectiveness of this approach is further demonstrated by the SNR improvements shown in Fig. S7.

Table 5 Summary of existing denoising methods.

References	Denoising method	Used Sentinel-2 band
Varon et al. (2021)	3×3 median filter & background mask: [methane enhancement > 95th percentile]	---
Ehret et al. (2022)	Gaussian filter & 5% worst prediction pixels	b11, b12
Zortea et al. (2023)	Gaussian filter & water body mask: [MNDWI >0.2]	b3, b12
This study	LRAD	b4, b8, b11, b12

6.2 Comparison with existing methane detectors

Multispectral satellite instruments such as Sentinel-2 record high-spatial-resolution global data, potentially capturing methane plume signals from numerous super-emitters. It poses great challenges to detect methane plumes from vast areas with various background noises relying on visual inspection, as well as to extensively annotate real-world training data for constructing automated detectors. Recently, various deep learning architectures have demonstrated feasibility for the automated detection of methane super-emissions in satellite imagery, including the vision transformer based network (Rouet-Leduc and Hulbert 2024), U-Net based models (Bruno et al., 2023; Vaughan et al., 2024), ResNet-50 (Zortea et al., 2023), EfficientNet-V2L (Radman et al., 2023), and MethaNet (Jongaramrungruang et al., 2022), a specialized network for methane detection. Most existing detectors require huge-volume simulated or synthetic datasets, the size of which is more than 100 times larger than the real data used to

https://doi.org/10.5194/egusphere-2024-2565
Preprint. Discussion started: 3 September 2024

train our methane detector.

While works in a data-efficient manner, our transferable DSAN method demonstrates lower false positive rates than existing detectors also trained with real data (Section 5). These detectors possibly degrade performances on test sets, due to the potential domain shift arising from spatiotemporal variations in real environment (Fig.10). In contrast, the specialized domain adaptation architecture in our detector can bridge such domain shift, making it promising for cost-effective and large-scale methane super-emitters detection. Once ΔR imagery with labeled information from one methane point source is available, the DSAN model can learn the plume/noise feature representation and transfer to other geographic regions with similar or even different environmental conditions.

6.3 Limitations and future enhancements

It should be noted that while the LRAD algorithm could effectively remove most artifacts presenting low reflectance values in methane-sensitive bands, but its robustness to remove plume-like artifacts in complex situations (see Fig. 13(a)) needs to be improved in future studies. Our real-world application in Hassi Messaoud reported a relatively high number of 336 false positive out of 3527 classifications. Most false positives were caused by artifacts that spectrally overlapped with methane absorption. This result suggests that more work is needed to eliminate these artifacts, especially those originating from surface features (account for 77.61%), to reduce the false positive rate of the Sentinel-2 monitoring workflow. Considering that land-surface type artifacts (from built-up areas and natural low-reflectivity surfaces) are spatially invariant, hyperspectral or radar satellite observations can be used to pre-identify potential

https://doi.org/10.5194/egusphere-2024-2565
Preprint. Discussion started: 3 September 2024

artifacts in oil and gas fields. Both of them excel at discriminating among various built-up structures and materials properties (Kuras et al. 2021). For key oil and gas fields with high emission frequencies, an artifact library can even be constructed so that Sentinel-2 can directly look up for regional masking when detecting methane sources. Furthermore, applications in more O&G fields would be needed for methane ultra-emitter monitoring. Augmentation of the true and diverse methane plume datasets can lead to better generalization capabilities of the detection model, while the time and labor costs of annotating plume-containing images need to be considered.

7. Conclusions

Here, we proposed a novel deep-transfer-learning-based approach that combined an adaptive artifacts removal algorithm (LRAD) with a transferable plume detector (DSAN), to identify methane-plume-containing images retrieved from Sentinel-2 observations. Our evaluation demonstrated that the proposed method efficiently detects plumes in different O&G fields. Applying the method to the Hassi Messaoud O&G field over a 1-year period discovered 33 anomalous emission events from three methane super-emitters, which were attributed to well blowout, pipeline leak, and unknown facility with average emission rates of 31133 kg/h, 3990 kg/h and 8210 kg/h, respectively.

The LRAD algorithm utilized Sentinel-2 bands 3, 8, 11, and 12 to remove multi-type artifacts associated with low reflectance in methane-sensitive bands, which greatly improved feature extraction by the deep model especially in heterogeneous regions of O&G fields. We applied the LRAD algorithm to ΔR retrieval from Sentinel-2 observations and compiled ΔR

https://doi.org/10.5194/egusphere-2024-2565
Preprint. Discussion started: 3 September 2024

datasets (1627 images in total) that include six different O&G super-emitters. The six labelled datasets have various ratios of positive (plume-containing) to negative (plume-free) sample size, plume sizes, and background noises.

The DSAN model was used to detect methane point sources based on ΔR images, aiming to resolving challenges arising from the domain shift between Sentinel-2 ΔR images for methane sources in different regions. For transfer detection tasks across six known methane sources, the DSAN model achieved an average macro-F1 score of 0.86, outperforming MethaNet and ResNet-50. Without a need for a huge volume of training data, our DSAN model operated in a data-efficient manner which leveraged knowledge acquired from a source domain during the training process to perform plume classification in a target domain.

Moving forward, the developed workflow can be modified to detect methane from other multispectral instruments, including Sentinel-2, LandSat-8, and WorldView-3. Also, it has the potential for detecting plumes of other pollutants observable by satellites such as NO_2 or CO_2. Moreover, while this study made efforts to develop a labelling decision rule, the confidence of the labels determined by human analysts was difficult to quantify. To facilitate robust algorithm development, we recommend the development of standards for plume identification and construction of benchmark plume datasets for varied satellite instruments.

Data availability

The six compiled methane retrieval ΔR datasets will be made available through a public repository upon publication [https://doi.org/10.57760/sciencedb.15792].

CRediT author statement

https://doi.org/10.5194/egusphere-2024-2565
Preprint. Discussion started: 3 September 2024

Shutao Zhao: Conceptualization, Methodology, Data curation, Software, Visualization, Writing-Original draft preparation. **Yuzhong Zhang:** Conceptualization, Investigation, Supervision, Validation, Writing-Original draft preparation, Funding. **Shuang Zhao:** Funding. **Xinlu Wang:** Reviewing and Editing. **Daniel J. Varon:** Software, Reviewing and Editing.

Declaration of Competing Interest

The authors declare that they have no known competing financial interests or personal relationships that could have appeared to influence the work reported in this paper.

Acknowledgements

This work was funded by the National Key Research and Development Program of China (2022YFE0209100), the National Natural Science Foundation of China (42307129), and the Zhejiang Provincial Natural Science Foundation (LZJMZ24D050005).

References

Biermann, L., Clewley, D., Martinez-Vicente, V., & Topouzelis, K. (2020). Finding Plastic Patches in Coastal Waters using Optical Satellite Data. *Scientific Reports, 10*, 5364

Buda Mateusz, Maki Atsuto, & A., M.M. (2018). A systematic study of the class imbalance problem in convolutional neural networks. *Neural Networks, 106*, 249-259

Burke, M., Driscoll, A., Lobell, D.B., & Ermon, S. (2021). Using satellite imagery to understand and promote sustainable development. *Science, 371*, eabe8628

Cusworth, D.H., Jacob, D.J., Varon, D.J., Chan Miller, C., Liu, X., Chance, K., Thorpe, A.K., Duren, R.M., Miller, C.E., Thompson, D.R., Frankenberg, C., Guanter, L., & Randles, C.A. (2019). Potential of next-generation imaging spectrometers to detect and quantify methane point sources from space. *Atmos. Meas. Tech., 12*, 5655-5668

Dodge, S., & Karam, L. (2016). Understanding how image quality affects deep neural networks. In, *2016 Eighth International Conference on Quality of Multimedia Experience (QoMEX)* (pp. 1-6)

Duren, R.M., Thorpe, A.K., Foster, K.T., Rafiq, T., Hopkins, F.M., Yadav, V., Bue, B.D., Thompson, D.R., Conley, S., Colombi, N.K., Frankenberg, C., McCubbin, I.B., Eastwood, M.L., Falk, M., Herner, J.D., Croes, B.E., Green, R.O., & Miller, C.E. (2019). California's methane super-emitters. *Nature, 575*, 180-184

Ehret, T., De Truchis, A., Mazzolini, M., Morel, J.-M., d'Aspremont, A., Lauvaux, T., Duren, R., Cusworth, D., & Facciolo, G. (2022). Global Tracking and Quantification of Oil and Gas Methane

https://doi.org/10.5194/egusphere-2024-2565
Preprint. Discussion started: 3 September 2024

Emissions from Recurrent Sentinel-2 Imagery. *Environmental Science & Technology, 56*, 10517-10529

Fan, X., Liu, Y., Wu, G., & Zhao, X. (2020). Compositing the Minimum NDVI for Daily Water Surface Mapping. In, *Remote Sensing*

Finch, D.P., Palmer, P.I., & Zhang, T. (2022). Automated detection of atmospheric NO2 plumes from satellite data: a tool to help infer anthropogenic combustion emissions. *Atmos. Meas. Tech., 15*, 721-733

Frankenberg, C., Thorpe, A.K., Thompson, D.R., Hulley, G., Kort, E.A., Vance, N., Borchardt, J., Krings, T., Gerilowski, K., Sweeney, C., Conley, S., Bue, B.D., Aubrey, A.D., Hook, S., & Green, R.O. (2016). Airborne methane remote measurements reveal heavy-tail flux distribution in Four Corners region. *Proceedings of the National Academy of Sciences, 113*, 9734-9739

Gorroño, J., Varon, D.J., Irakulis-Loitxate, I., & Guanter, L. (2023). Understanding the potential of Sentinel-2 for monitoring methane point emissions. *Atmos. Meas. Tech., 16*, 89-107

Guanter, L., Irakulis-Loitxate, I., Gorroño, J., Sánchez-García, E., Cusworth, D.H., Varon, D.J., Cogliati, S., & Colombo, R. (2021). Mapping methane point emissions with the PRISMA spaceborne imaging spectrometer. *Remote Sensing of Environment, 265*, 112671

Ienco, D., Interdonato, R., Gaetano, R., & Ho Tong Minh, D. (2019). Combining Sentinel-1 and Sentinel-2 Satellite Image Time Series for land cover mapping via a multi-source deep learning architecture. *ISPRS Journal of Photogrammetry and Remote Sensing, 158*, 11-22

Iman, M., Arabnia, H.R., & Rasheed, K. (2023). A Review of Deep Transfer Learning and Recent Advancements. In, *Technologies*

Irakulis-Loitxate, I., Guanter, L., Maasakkers, J.D., Zavala-Araiza, D., & Aben, I. (2022). Satellites Detect Abatable Super-Emissions in One of the World's Largest Methane Hotspot Regions. *Environmental Science & Technology, 56*, 2143-2152

Jiang, J., Shu, Y., Wang, J., & Long, M. (2022). Transferability in deep learning: A survey. *arXiv preprint arXiv:.05867*

Johnson Justin M., & M., K. (2019). Survey on deep learning with class imbalance. *Journal of Big Data, 6*, 27

Jongaramrungruang, S., Thorpe, A.K., Matheou, G., & Frankenberg, C. (2022). MethaNet – An AI-driven approach to quantifying methane point-source emission from high-resolution 2-D plume imagery. *Remote Sensing of Environment, 269*, 112809

Kuc, G., & Chormański, J. (2019). SENTINEL-2 IMAGERY FOR MAPPING AND MONITORING IMPERVIOUSNESS IN URBAN AREAS. *Int. Arch. Photogramm. Remote Sens. Spatial Inf. Sci., XLII-1/W2*, 43-47

Kuras, A., Brell, M., Rizzi, J., & Burud, I. (2021). Hyperspectral and Lidar Data Applied to the Urban Land Cover Machine Learning and Neural-Network-Based Classification: A Review. In, *Remote Sensing*

Laurens van der Maaten, & Hinton, G. (2008). Visualizing data using t-SNE. *Journal of machine learning research, 9*, 2579−2605

Lauvaux, T., Giron, C., Mazzolini, M., d'Aspremont, A., Duren, R., Cusworth, D., Shindell, D., & Ciais, P. (2022). Global assessment of oil and gas methane super-emitters. *Science, 375*, 557-561

Lee, H., Park, M., & Kim, J. (2016). Plankton classification on imbalanced large scale database via convolutional neural networks with transfer learning. In, *2016 IEEE International Conference on Image Processing (ICIP)* (pp. 3713-3717)

Liu, Y., Zhi, W., Xu, B., Xu, W., & Wu, W. (2021). Detecting high-temperature anomalies from Sentinel-2 MSI images. *ISPRS Journal of Photogrammetry and Remote Sensing, 177*, 174-193

Naus, S., Maasakkers, J.D., Gautam, R., Omara, M., Stikker, R., Veenstra, A.K., Nathan, B., Irakulis-

https://doi.org/10.5194/egusphere-2024-2565
Preprint. Discussion started: 3 September 2024

Loitxate, I., Guanter, L., Pandey, S., Girard, M., Lorente, A., Borsdorff, T., & Aben, I. (2023). Assessing the Relative Importance of Satellite-Detected Methane Superemitters in Quantifying Total Emissions for Oil and Gas Production Areas in Algeria. *Environmental Science & Technology, 57*, 19545-19556

Ma, Y., Chen, S., Ermon, S., & Lobell, D.B. (2024). Transfer learning in environmental remote sensing. Remote Sensing of Environment, 301, 113924

Pan, S.J., & Yang, Q. (2010). A Survey on Transfer Learning. *IEEE Transactions on Knowledge and Data Engineering, 22*, 1345-1359

Pandey, S., van Nistelrooij, M., Maasakkers, J.D., Sutar, P., Houweling, S., Varon, D.J., Tol, P., Gains, D., Worden, J., & Aben, I. (2023). Daily detection and quantification of methane leaks using Sentinel-3: a tiered satellite observation approach with Sentinel-2 and Sentinel-5p. *Remote Sensing of Environment, 296*, 113716

Pedregosa, F., Varoquaux, G., Gramfort, A., Michel, V., Thirion, B., Grisel, O., Blondel, M., Prettenhofer, P., Weiss, R., & Dubourg, V. (2011). Scikit-learn: Machine learning in Python. *Journal of machine Learning research, 12*, 2825-2830

Purio, M.A., Yoshitake, T., & Cho, M. (2022). Assessment of Intra-Urban Heat Island in a Densely Populated City Using Remote Sensing: A Case Study for Manila City. In, *Remote Sensing*

Radman, A., Mahdianpari, M., Varon, D.J., & Mohammadimanesh, F. (2023). S2MetNet: A novel dataset and deep learning benchmark for methane point source quantification using Sentinel-2 satellite imagery. *Remote Sensing of Environment, 295*, 113708

Rouet-Leduc, B., & Hulbert, C. (2024). Automatic detection of methane emissions in multispectral satellite imagery using a vision transformer. Nature Communications, 15, 3801

Ramoelo, A., Cho, M., Mathieu, R., & Skidmore, A. (2015). Potential of Sentinel-2 spectral configuration to assess rangeland quality, *Journal of Applied Remote Sensing*, 094096

Sánchez-García, E., Gorroño, J., Irakulis-Loitxate, I., Varon, D.J., & Guanter, L. (2022). Mapping methane plumes at very high spatial resolution with the WorldView-3 satellite. *Atmos. Meas. Tech., 15*, 1657-1674

Schuit, B.J., Maasakkers, J.D., Bijl, P., Mahapatra, G., Van den Berg, A.W., Pandey, S., Lorente, A., Borsdorff, T., Houweling, S., Varon, D.J., McKeever, J., Jervis, D., Girard, M., Irakulis-Loitxate, I., Gorroño, J., Guanter, L., Cusworth, D.H., & Aben, I. (2023). Automated detection and monitoring of methane super-emitters using satellite data. *Atmos. Chem. Phys. Discuss., 2023*, 1-47

Varghese, D., Radulović, M., Stojković, S., & Crnojević, V. (2021). Reviewing the Potential of Sentinel-2 in Assessing the Drought*, 13*, 3355

Varon, D.J., Jacob, D.J., Jervis, D., & McKeever, J. (2020). Quantifying Time-Averaged Methane Emissions from Individual Coal Mine Vents with GHGSat-D Satellite Observations. *Environmental Science & Technology, 54*, 10246-10253

Varon, D.J., Jacob, D.J., McKeever, J., Jervis, D., Durak, B.O.A., Xia, Y., & Huang, Y. (2018). Quantifying methane point sources from fine-scale satellite observations of atmospheric methane plumes. *Atmos. Meas. Tech., 11*, 5673-5686

Varon, D.J., Jervis, D., McKeever, J., Spence, I., Gains, D., & Jacob, D.J. (2021). High-frequency monitoring of anomalous methane point sources with multispectral Sentinel-2 satellite observations. *Atmos. Meas. Tech., 14*, 2771-2785

Vaughan, A., Mateo-García, G., Gómez-Chova, L., Růžička, V., Guanter, L., & Irakulis-Loitxate, I. (2023). CH4Net: a deep learning model for monitoring methane super-emitters with Sentinel-2 imagery. *EGUsphere, 2023*, 1-17

Yuan, Q., Shen, H., Li, T., Li, Z., Li, S., Jiang, Y., Xu, H., Tan, W., Yang, Q., Wang, J., Gao, J., & Zhang, L. (2020). Deep learning in environmental remote sensing: Achievements and challenges. *Remote Sensing of Environment, 241*, 111716

Zavala-Araiza, D., Alvarez, R.A., Lyon, D.R., Allen, D.T., Marchese, A.J., Zimmerle, D.J., & Hamburg, S.P. (2017). Super-emitters in natural gas infrastructure are caused by abnormal process conditions. *Nature Communications, 8*, 14012

Zhang, Z., Sherwin, E.D., Varon, D.J., & Brandt, A.R. (2022). Detecting and quantifying methane emissions from oil and gas production: algorithm development with ground-truth calibration based on Sentinel-2 satellite imagery. *Atmos. Meas. Tech., 15*, 7155-7169

Zhou, W., Bovik, A.C., Sheikh, H.R., & Simoncelli, E.P. (2004). Image quality assessment: from error visibility to structural similarity. *IEEE Transactions on Image Processing, 13*, 600-612

Zhu, Y., Zhuang, F., Wang, J., Ke, G., Chen, J., Bian, J., Xiong, H., & He, Q. (2021). Deep Subdomain Adaptation Network for Image Classification. *IEEE Transactions on Neural Networks and Learning Systems, 32*, 1713-1722

Zortea, M., Almeida, J.L.D.S., Klein, L., & Junior, A.C.N. (2023). Detection of methane plumes using Sentinel-2 satellite images and deep neural networks trained on synthetically created label data. In, 2023 IEEE International Conference on Big Data (BigData) (pp. 3830-3839)